The effect of compressibility on the stability of wall-bounded Kolmogorov flow

A. Manela and J. Zhang

Journal of Fluid Mechanics / Volume 694 / March 2012, pp 29 - 49
DOI: 10.1017/jfm.2011.499, Published online: 31 January 2012

J. Fluid Mech. (2012), *vol.* 694, *pp.* 29–49.
doi:10.1017/jfm.2011.499

The effect of compressibility on the stability of wall-bounded Kolmogorov flow

A. Manela[1] **and J. Zhang**[2]†

[1] Faculty of Aerospace Engineering, Technion, Israel Institute of Technology, Haifa 32000, Israel

[2] Laboratory of High Temperature Gas Dynamics, Institute of Mechanics, Chinese Academy of Sciences, Beijing 100190, China

(Received 21 July 2011; revised 9 October 2011; accepted 7 November 2011; first published online 31 January 2012)

We extend the stability analysis of incompressible Kolmogorov flow, induced by a spatially periodic external force in an unbounded domain, to a compressible hard-sphere gas confined between two parallel isothermal walls. The two-dimensional problem is studied by means of temporal stability analysis of a 'slip flow' continuum-limit model and the direct simulation Monte Carlo (DSMC) method. The neutral curve is obtained in terms of the Reynolds (Re) and Knudsen (Kn) numbers, for a given non-dimensional wavenumber ($2\pi n$) of the external force. In the incompressible limit ($Kn, Kn\,Re \to 0$), the problem is governed only by the Reynolds number, and our neutral curve coincides with the critical Reynolds number (Re_{cr}) calculated in previous incompressible analyses. Fluid compressibility ($Kn, Kn\,Re \neq 0$) affects the flow field through the generation of viscous dissipation, coupling flow shear rates with irreversible heat production, and resulting in elevated bulk-fluid temperatures. This mechanism has a stabilizing effect on the system, thus increasing Re_{cr} (compared to its incompressible value) with increasing Kn. When compressibility effects become strong enough, transition to instability changes type from 'exchange of stabilities' to 'overstability', and perturbations are dominated by fluctuations in the thermodynamic fields. Most remarkably, compressibility confines the instability to small ($O(10^{-3})$) Knudsen numbers, above which the Kolmogorov flow is stable for all Re. Good agreement is found between 'slip flow' and DSMC analyses, suggesting the former as a useful alternative in studying the effects of various parameters on the onset of instability, particularly in the context of small Knudsen numbers considered.

Key words: gas dynamics, instability, rarefied gas flow

1. Introduction

The Kolmogorov flow, a unidirectional shear flow induced by a spatially periodic external force, has been suggested by Kolmogorov as a model problem for studying hydrodynamic stability and transition phenomena (Arnol'd & Meshalkin 1960). Ever since, the Kolmogorov flow has been investigated in a large number of works, both theoretically and experimentally. Meshalkin & Sinai (1961) were the first to analyse the linear stability problem in an unbounded domain, and obtained the critical

† Email address for correspondence: zhangjun04@imech.ac.cn

Reynolds number for instability. It was found that instability sets in at a critical Reynolds number of $\sqrt{2}$ in the form of infinitely long stationary waves. Green (1974), Sivashinsky (1985), She (1987) and Platt, Sirovich & Fitzmaurice (1991), among others, studied the problem at higher Reynolds numbers, and examined the onset of secondary instability and transition to turbulence. To inspect the theoretical results in experiments, several works have studied the stability problem in magnetohydrodynamic fluids (Sommeria 1986; Tabeling, Perrin & Fauve 1987) and soap-film flow systems (Burgess *et al.* 1999).

Realization of the Kolmogorov flow in experiments made it necessary to consider a finite domain and introduce boundaries, which were not included in early idealized theories. According to experimental observations, the presence of solid boundaries stabilizes the reference flow (i.e. increases the critical Reynolds number) and results in a finite critical wavelength of perturbations. Thess (1992) studied the effect of confining boundaries in numerical simulations by imposing no-penetration and perfect-slip (no tangent vorticity) conditions at the walls. The latter condition was preferred over the no-slip condition to ensure a non-singular behaviour of the numerical scheme. Later on, Fukuta & Murakami (1998) analysed the problem with no-slip boundary conditions and investigated the finite-wave onset of instability. It was found that, in the limit where the external force wavelength is much smaller than the distance between the walls, the effect of boundaries vanishes and the critical conditions converge to the unbounded-domain result.

All the above works have considered the case of an incompressible fluid only. In particular, no systematic analysis has been carried out to study the combined effect of fluid compressibility and domain-boundedness on the stability of the Kolmogorov flow. To the best of our knowledge, the effect of fluid compressibility on the stability problem was only considered by Bena, Malek Mansour & Baras (1999). While their analysis allows for non-zero density and pressure perturbations, it assumes an incompressible reference state and isothermal conditions throughout the fluid domain. The main objective of the present work is therefore to systematically account for the impact of compressibility on the stability of bounded Kolmogorov flow, with no *a priori* restrictions on the coupling between the dynamic and thermodynamic descriptions of the fluid. We consider the case of an ideal gas, and allow for non-zero rarefaction rates to take place through the combined influences of gas viscosity and compressibility.

Stability analyses of rarefied gas flows have appeared in the literature since the 1990s, motivated by the interest in relating mechanisms of instability and self-organization at the molecular level with macroscopic phenomena. Existing works have focused on the canonical Rayleigh–Bénard (Golshtein & Elperin 1996; Stefanov, Roussinov & Cercignani 2002; Zhang & Fan 2009) and Taylor–Couette (Stefanov & Cercignani 1993) problems, and were initially based on the direct simulation Monte Carlo (DSMC) method (Bird 1994). Typically, instability phenomena were confined in all cases to the 'continuum limit' of small Knudsen numbers. However, in this limit the DSMC method becomes prohibitively time-consuming. Several contributions have therefore applied an alternative approach, the 'slip flow' continuum-limit model, based on the Navier–Stokes equations with velocity slip and temperature jump boundary conditions, to solve the problems in hand. The flow problems were analysed either using finite-difference schemes of the full nonlinear model (Stefanov *et al.* 2002; Stefanov, Roussinov & Cercignani 2007), or by means of linear temporal stability schemes (Manela & Frankel 2005, 2007; Yoshida & Aoki 2006), and supplied results that were in good agreement with DSMC predictions. In addition to the considerably

less demanding calculation, the linear stability analysis yielded unequivocal results for the critical conditions for instability, contrary to DSMC predictions, which become particularly noisy close to marginal stability conditions (see § 3). The main deficiency of linear stability analysis is in not yielding the 'final state' of perturbations. (Even at slightly supercritical conditions, a complex system behaviour was found in previous analyses, which could not be predicted using linear investigation – see e.g. Stefanov *et al.* (2007), who found a cascade of instabilities close to the critical system conditions in the three-dimensional Rayleigh–Bénard problem.) To capture the terminal state of the system, a nonlinear investigation must be carried out. Bearing in mind this restriction, we follow here the linear stability scheme of solution for the purpose of delineating the domain of instability and characterizing the onset of critical perturbations in the compressible Kolmogorov problem.

The stability of the Kolmogorov flow in rarefied gases has been considered by Zhang & Fan (2011) using the DSMC method. However, the thermodynamic state of the system was artificially decoupled from the dynamical problem by imposing isothermal conditions in the simulation and periodic boundaries in all directions. In the present contribution, we relax this assumption by studying the stability of the fully coupled viscous–compressible Kolmogorov flow. Most importantly, the full reference compressible flow problem is governed by a balance between fluid heat conduction and viscous dissipation, which yields a solution much different from the counterpart incompressible result. As will be demonstrated, the effect of fluid dissipation, neglected in previous works, has a strong stabilizing impact on the system.

The paper outline is as follows. In §§ 2 and 3 the general 'slip flow' problem and numerical DSMC scheme are described, respectively. The reference Kolmogorov flow is calculated in § 4, and its linear stability is studied in § 5. In § 6 the perturbation flow field in the unstable domain is discussed, and in § 7 the case of large forcing wavenumbers is considered. Concluding comments are given in § 8.

2. Formulation of the 'slip flow' problem

Consider a two-dimensional set-up of a perfect monatomic hard-sphere gas confined between two infinitely long parallel walls. The walls are separated by a distance L and maintained at a fixed and uniform temperature T_0. The gas is subject to a spatially periodic body force per unit mass of amplitude F_0 in a direction $\hat{\boldsymbol{x}}_1$ parallel to the walls. In a non-dimensional form,

$$\boldsymbol{F} = \sin(2\pi n x_2)\,\hat{\boldsymbol{x}}_1, \tag{2.1}$$

where the force is scaled by F_0, $2\pi n$ is the non-dimensional force wavenumber, and x_2, scaled by L, is measured normal to the walls located at $x_2 = 0$ and $x_2 = 1$. Following previous incompressible analyses, we take n to be a positive integer so that the force vanishes at the walls.

The 'slip flow' problem is governed by the Navier–Stokes–Fourier equations together with the equation of state for a compressible hard-sphere gas. To render the problem dimensionless, we normalize the position vector by L, the gas density by its mean value ρ_0, the temperature by T_0, and the pressure by $\rho_0 R T_0$ (wherein R denotes the gas constant). The shear viscosity and heat conductivity are normalized by μ_0 and κ_0, their respective values at T_0, and the velocity is scaled by $U_0 = \rho_0 F_0 L^2/\mu_0$, associated with the magnitude of the external force. The resulting dimensionless

problem consists of the continuity

$$\frac{\partial \rho}{\partial t} + \nabla \cdot (\rho \boldsymbol{u}) = 0, \tag{2.2}$$

momentum

$$\rho \frac{\mathrm{D}\boldsymbol{u}}{\mathrm{D}t} = -\frac{1}{\gamma Ma^2}\nabla p + \frac{1}{Re_L}\nabla \cdot \boldsymbol{p} + \frac{1}{Re_L}\rho \boldsymbol{F} \tag{2.3}$$

and energy

$$\rho \frac{\mathrm{D}T}{\mathrm{D}t} = \frac{\gamma}{PrRe_L}\nabla \cdot \boldsymbol{q} - (\gamma - 1)p\nabla \cdot \boldsymbol{u} + \gamma(\gamma - 1)\frac{Ma^2}{Re_L}\Phi \tag{2.4}$$

equations, as well as the perfect gas equation of state

$$p = \rho T. \tag{2.5}$$

In the above,

$$\boldsymbol{p} = \mu[\nabla \boldsymbol{u} + (\nabla \boldsymbol{u})^{\dagger} - \tfrac{2}{3}\nabla \cdot \boldsymbol{u}\boldsymbol{I}] \tag{2.6}$$

is the Newtonian deviatoric stress,

$$\boldsymbol{q} = -\kappa \nabla T \tag{2.7}$$

is the heat flux density satisfying the Fourier law, and $\Phi = \boldsymbol{p} : \nabla \boldsymbol{u}$ is the rate of viscous dissipation. Also appearing in (2.3) and (2.4) are the Reynolds and Mach numbers,

$$Re_L = \rho_0 U_0 L/\mu_0, \quad Ma = U_0/\sqrt{\gamma RT_0}, \tag{2.8}$$

with $\gamma = c_p/c_v$ denoting the ratio of specific heats at constant pressure and constant volume, respectively, and the Prandtl number, $Pr = \mu_0 c_p/\kappa_0$. For a hard-sphere gas, $\gamma = 5/3$, $Pr = 2/3$ and

$$\mu, \kappa = \sqrt{T} \tag{2.9}$$

(Sone 2002). The above equations are supplemented by a normalization condition

$$\int \rho \, \mathrm{d}\boldsymbol{x} = 1, \tag{2.10}$$

specifying the total amount of gas between the walls, and by the boundary conditions

$$u_2 = 0, \quad u_1 = \pm\zeta \frac{\partial u_1}{\partial x_2}, \quad T = 1 \pm \tau \frac{\partial T}{\partial x_2} \quad \text{at } x_2 = \begin{bmatrix} 0 \\ 1 \end{bmatrix}, \tag{2.11}$$

imposing the vanishing of the normal velocity component and designating the magnitudes of velocity slip and temperature jump at the walls, respectively. In (2.11), $\zeta = 1.1466Kn$, $\tau = 2.1269Kn$ and $Kn = l/L$ is the Knudsen number, where $l = 16\mu_0/(5\rho_0\sqrt{2\pi RT_0})$ is the mean free path of a gas molecule at the reference conditions (Sone 2002). For a hard-sphere gas, the Knudsen, Mach and Reynolds numbers are correlated through the *von Kármán relation* (Tsien 1946; von Kármán 1963),

$$Kn = \frac{16}{\sqrt{30\pi}}\frac{Ma}{Re_L}. \tag{2.12}$$

For later convenience, subsequent results will be presented in terms of a modified Reynolds number,

$$Re = \frac{Re_L}{8\pi^3 n^3}, \tag{2.13}$$

identical with the definition used in incompressible analyses (Green 1974).

3. Monte Carlo simulations

The prevalent numerical scheme for simulating the motion of a rarefied gas is the direct simulation Monte Carlo (DSMC) method (Bird 1994). The fundamental idea of DSMC is to track a large number of representative molecules, with their motions and intermolecular collisions assumed uncoupled during small time intervals. Molecular motions are modelled deterministically, while molecular collisions are treated statistically. With the gradual increase in computational power, DSMC has been applied to simulate flows in the near-continuum limit of small Knudsen numbers.

We apply a standard DSMC algorithm to simulate Kolmogorov flow of a hard-sphere gas confined in a two-dimensional rectangle of width L and length D, with aspect ratio $D/L = 2$. The hard-sphere model is chosen for simplicity of calculation. In accordance with the problem set-up, the bounding walls at $x_2 = 0$ and $x_2 = 1$ are fixed at a constant temperature and assumed to be fully accommodating. Periodicity conditions are prescribed on the walls at $x_1 = 0$ and $x_1 = D/L = 2$. The latter conditions restrict the spectrum of perturbation wavenumbers to a discrete spectrum. For the chosen aspect ratio $D/L = 2$, only perturbations with wavenumbers $k = \pi n$ ($n = 1, 2, \ldots$) are allowed. As will be shown in § 5, the impact of this restriction on the results (compared to the 'slip flow' scheme, where a continuous spectrum is considered) is minor.

To carry out a simulation, the gas is set at quiescent initial conditions and in thermodynamic equilibrium with the boundaries. The computation domain is divided into 128×128 sampling cells. At $t = 0$ the external force is applied and the flow field is followed through its terminal state. Each cell is divided into square subcells, within which collision pairs are selected. In cases where there are not enough molecules to perform collisions in a particular subcell, a layered search algorithm in neighbouring subcells is adopted to make neighbouring molecules be picked preferentially for collisions (Bird 1994). The side length of subcells is $l/3$ (where l is the mean free path of a gas molecule), which is found to be sufficient for convergence of the results. Depending on the Knudsen number, the total number of simulation molecules is varied between 5.0×10^6 for $Kn = 0.004$ to 2.0×10^7 for $Kn = 0.002$. The calculation time step is $\mathrm{d}t = 0.1\tau$, where τ denotes the mean collision time of a molecule. In each time step, a velocity increment of $F_0 \sin(2\pi n x_2)\,\mathrm{d}t$ (see (2.1)) is added to the velocity in the x_1 direction, to account for external forcing. Time averaging is used to examine the evolution of the macroscopic fields, where each time average contains 10^3 computation time steps. Each simulation proceeded until a stationary or time-periodic state was achieved. In all cases examined, the terminal state did not exhibit any quasi- or non-periodic time variations.

To examine whether instability occurs at a specific set of parameters, the time and space deviations of the macroscopic fields from their mean values were examined. Cases where obvious convective patterns were formed were categorized 'unstable', while parameter combinations where the macroscopic velocity in the x_2 direction was found to be small and 'random' were classified 'stable'. In addition, the final 'stable'

states were compared with the reference 'slip flow' solution (see § 4) to confirm that the numerical results indeed converged to the steady reference state.

Exact delineation of the instability domain based on DSMC results is a formidable task, particularly since, for parameter combinations in the vicinity of the onset of instability, the statistical noise inherent in the results is of the same order of magnitude as the physical signal. Furthermore, DSMC calculations become extremely time-consuming in the continuum limit, where a large number of simulation particles are required for the computation. Our DSMC results are therefore considered as a complementary tool to validate the 'slip flow' analysis. Unlike DSMC, the 'slip flow' model supplies unequivocal predictions for the onset of instability, as mentioned in the Introduction.

4. The reference Kolmogorov flow

The reference state is a steady bounded Kolmogorov flow wherein $\boldsymbol{u}^{(\mathbf{0})} = (u^{(0)}, 0)$, the velocity vector, as well as $T^{(0)}$, $\rho^{(0)}$ and $p^{(0)}$ are assumed to be functions of the normal coordinate x_2 only. In this case the equation of continuity (2.2) is satisfied identically and the x_2 component of the momentum equation (2.3) yields a constant reference pressure $p^{(0)} = C$. Applying the equation of state (2.5) to express $\rho^{(0)} = C/T^{(0)}$, the remaining x_1 momentum and energy equations yield a system of nonlinear coupled equations for $u^{(0)}$ and $T^{(0)}$,

$$\frac{\mathrm{d}}{\mathrm{d}x_2}\left(\sqrt{T^{(0)}}\,\frac{\mathrm{d}u_1^{(0)}}{\mathrm{d}x_2}\right) + \frac{C}{T^{(0)}}\sin(2\pi n x_2) = 0, \tag{4.1}$$

representing a balance between viscous shear stress and external force, and

$$\frac{\mathrm{d}}{\mathrm{d}x_2}\left(\sqrt{T^{(0)}}\,\frac{\mathrm{d}T^{(0)}}{\mathrm{d}x_2}\right) + \frac{4Ma^2}{9}\sqrt{T^{(0)}}\left(\frac{\mathrm{d}u_1^{(0)}}{\mathrm{d}x_2}\right)^2 = 0, \tag{4.2}$$

expressing a balance between heat conduction and rate of viscous dissipation. The formulation of the reference-state problem is completed by imposing the normalization condition (2.10),

$$C = \left(\int_0^1 \frac{1}{T^{(0)}}\,\mathrm{d}x_2\right)^{-1}, \tag{4.3}$$

together with the velocity slip and temperature jump conditions obtained from (2.11),

$$u_1^{(0)} = \pm\zeta\,\frac{\mathrm{d}u_1^{(0)}}{\mathrm{d}x_2}, \quad T^{(0)} = 1 \pm \tau\,\frac{\mathrm{d}T^{(0)}}{\mathrm{d}x_2} \quad \text{at } x_2 = \begin{bmatrix} 0 \\ 1 \end{bmatrix}. \tag{4.4}$$

For given n, Ma and Kn, integration of the ordinary system of (4.1) and (4.2) together with conditions (4.3) and (4.4) yield $u_1^{(0)}$, $T^{(0)}$ and $C = p^{(0)}$. The reference density field is then given by $\rho^{(0)} = C/T^{(0)}$.

In the incompressible limit ($Ma, Kn \to 0$), the system (4.1)–(4.4) resolves into a momentum balance together with no-slip boundary conditions. The reference state then recovers its incompressible form (Meshalkin & Sinai 1961),

$$u_{1,incom}^{(0)} = \frac{\sin(2\pi n x_2)}{4\pi^2 n^2}, \quad T_{incom}^{(0)} = p_{incom}^{(0)} = \rho_{incom}^{(0)} = 1. \tag{4.5}$$

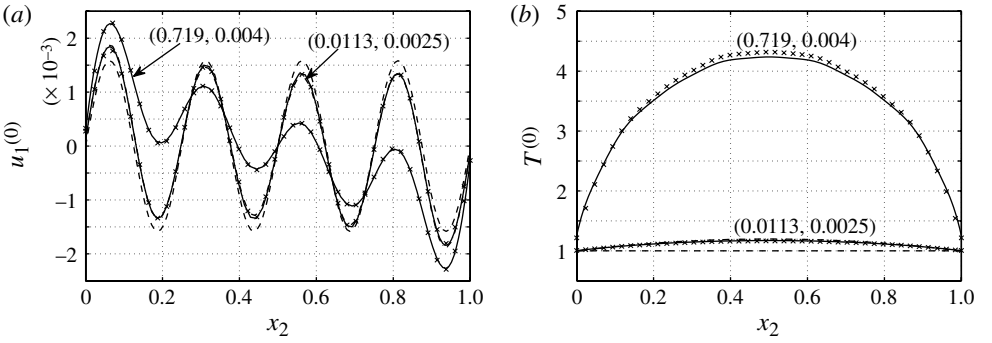

FIGURE 1. The reference (*a*) x_1 velocity and (*b*) temperature at the indicated (ε, Kn) combinations for $n = 4$. The solid lines correspond to 'slip flow' solution and the crosses mark DSMC data. The dashed lines depict the reference state in the incompressible case, and the dash-dotted lines (nearly coinciding with the exact 'slip flow' solution for $(\varepsilon, Kn) = (0.0113, 0.0025)$) show the asymptotic approximation for $\varepsilon, Kn \ll 1$.

Considering the case $Ma, Kn > 0$, compressibility affects the reference state primarily through the viscous dissipation term $O(Ma^2)$ in (4.2). The effect of *weak* compressibility can be examined analytically by considering small Kn and Ma fluctuations of the incompressible solution (4.5). Introducing

$$\varepsilon \equiv Ma^2/(16\pi^4 n^4), \tag{4.6}$$

expanding

$$F^{(0)}(x_2) \approx F^{(0)}_{incom}(x_2) + \varepsilon F^{(0)}_{\varepsilon}(x_2) + KnF^{(0)}_{Kn}(x_2) + O(\varepsilon^2, Kn^2, \varepsilon Kn) \tag{4.7}$$

(where $F^{(0)}$ represents any of the reference fields) and substituting (4.7) into (4.1)–(4.4) yields a system of linear equations for the $O(\varepsilon, Kn)$ terms. The first-order corrections for the reference velocity and temperature can then be found as

$$u^{(0)}_{1_\varepsilon} = a_1 x_2 + f(x_2), \quad u^{(0)}_{1_{Kn}} = b_1 x_2 + b_0 \tag{4.8}$$

and

$$T^{(0)}_{\varepsilon} = -\frac{4\pi^2 n^2}{9}\left[x_2^2 - x_2 + \frac{1-\cos(4\pi n x_2)}{8\pi^2 n^2}\right], \quad T^{(0)}_{Kn} = 0. \tag{4.9}$$

The constants a_1, b_1, b_0 and the function $f(x_2)$ in (4.8) are tabulated in appendix A. The effect of gas compressibility is mainly reflected through the parabolic non-uniformity of $T^{(0)}_{\varepsilon}$ in (4.9). This non-uniformity couples the $O(\varepsilon)$ correction $u^{(0)}_{1_\varepsilon}$ in (4.8), while $u^{(0)}_{1_{Kn}}$ originates from the slip boundary condition (4.4). The general solution of (4.1)–(4.4) for arbitrary n, ε and small Kn is computed numerically by means of MATLAB routines.

Figure 1 describes the effect of compressibility on the reference $u^{(0)}_1$ (figure 1*a*) and $T^{(0)}$ (figure 1*b*) fields for $n = 4$. The two $(\varepsilon, Kn) = (0.0113, 0.0025)$, $(0.719, 0.004)$ cases presented correspond to $Re \approx 2.79$ and $Re \approx 13.9$, respectively (see (2.12) and (2.13)). The solid lines are obtained via numerical integration of the full 'slip flow' model and the crosses mark the corresponding distributions obtained via DSMC calculations. The dashed lines present the incompressible solution (4.5), which depends

on n only. The dashed-dotted lines mark the $\varepsilon, Kn \ll 1$ approximations (4.7) at $(\varepsilon, Kn) = (0.0113, 0.0025)$.

With increasing ε, the velocity profile deviates from its incompressible sinusoidal shape to form a descending wave, asymmetric about $x_2 = 0.5$, and with maximum amplitudes in the vicinity of the walls. However, the main effect of gas compressibility on the reference state, as seen from figure 1(*b*), is to increase the bulk gas temperature through the mechanism of viscous dissipation. For the chosen $(\varepsilon, Kn) = (0.0113, 0.0025)$, (4.7) predicts well the velocity profile and the parabolic non-uniformity of the temperature distribution, which are nearly indiscernible from the exact solution. With the minor exception of $T^{(0)}$ in the middle portion of the gap, the 'slip flow' and Monte Carlo solutions nearly coincide, which supports the present use of the simplified near-continuum model.

While the Knudsen numbers considered are very small ($Kn \lesssim 0.004$), the effect of gas rarefaction becomes non-negligible with increasing ε, as reflected by the considerable temperature jump (of about 20 % in figure 1*b*) and velocity slip for $\varepsilon = 0.719$. This is because the *local* Knudsen number, based on the gradients of the hydrodynamic fields, becomes large with increasing ε, owing to the large dissipation rates in the vicinity of the walls. The local increase in Kn is taken into account in the velocity slip and temperature jump boundary conditions (4.4) through the product of the global Knudsen number with the local gradient of the respective hydrodynamic field at the boundary. With increasing ε at a given Kn, the temperature increase in the middle of the gap together with growing temperature jump at the walls become more and more pronounced. This is equivalent to increasing Re (the relative magnitude of external force) at a given Kn (see (2.12) and (2.13)), which amplifies the irreversible production of heat dissipation (see also the discussion pertaining to figure 2).

It is instructive to note the variation of the (constant) reference pressure with ε. In the incompressible limit, the uniform pressure is equal to unity (see (4.5)). With growing ε, the increase in mean gas temperature together with the preservation of mean gas density (see (2.10)) result in an increase in the reference pressure, in accordance with the equation of state (2.5). The approximate solution (4.7) in the limit $\varepsilon, Kn \ll 1$ yields

$$p^{(0)} \approx 1 + \frac{2\varepsilon}{9}\left(\frac{\pi^2 n^2}{3} - \frac{1}{4}\right) + O(\varepsilon^2, Kn^2, \varepsilon Kn), \tag{4.10}$$

in agreement with the exact solution for $(\varepsilon, Kn) = (0.0113, 0.0025)$, predicting $p^{(0)} \approx 1.13$. At $(\varepsilon, Kn) = (0.719, 0.004)$, the exact solution yields $p^{(0)} \approx 3.22$. This increase in $p^{(0)}$, a manifestation of conversion of gas kinetic energy into heat, has a stabilizing effect on the system, as will be demonstrated in § 5.

The above results could be described in terms of Ma instead of ε, as both represent the effect of gas compressibility. However, here we prefer the use of ε over Ma (being ≈ 67 for $\varepsilon = 0.0113$ and ≈ 536 for $\varepsilon = 0.719$), as the latter is misleadingly large, and does not reflect the actual value of gas velocity. As can be seen from the small $O(10^{-3})$ non-dimensional values of $u_1^{(0)}$ in figure 1(*a*), the gas velocity is always subsonic. In what follows, we therefore present our results in terms of the physically significant parameters Re, Kn and n; the respective values of Ma and ε can be found by simple manipulation of (2.12) and (2.13) and the definition of ε.

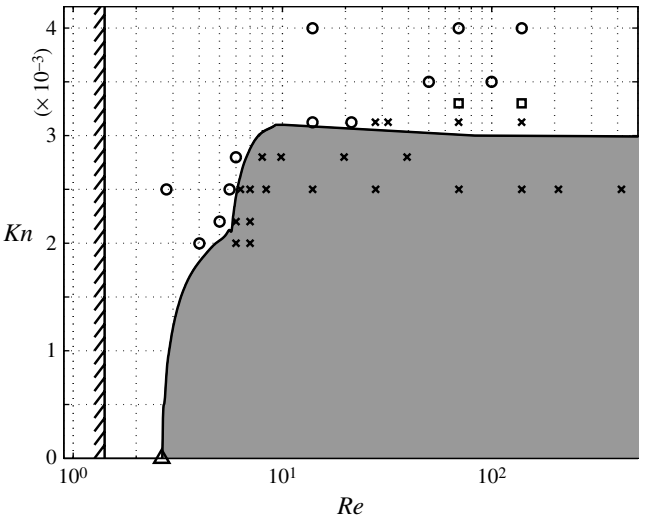

FIGURE 2. Division of the (Re, Kn) plane into domains of stable (unshaded) and unstable (shaded) response for $n = 4$ according to 'slip flow' stability analysis. The circles, crosses and squares mark parameter combinations where the reference state is stable, unstable and marginally stable, respectively, according to DSMC results. The cross-hatched line shows the critical Reynolds number in the incompressible unbounded problem ($Re_{cr} \approx \sqrt{2}$; Meshalkin & Sinai 1961), and the triangle indicates the critical value in the incompressible wall-bounded problem ($Re_{cr} \approx 2.65$; Fukuta & Murakami 1998).

5. Stability analysis

The linear temporal stability analysis of the reference Kolmogorov flow is studied by assuming that it is perturbed by small two-dimensional spatially harmonic perturbations. The above-mentioned fields are generically represented by the sum

$$F(x_1, x_2, t) = F^{(0)}(x_2) + \phi^{(1)}(x_2) \exp[\mathrm{i}(kx_1 + \omega t)], \tag{5.1}$$

wherein the real k and complex ω represent the perturbation wavenumber and its growth rate, respectively. Substituting (5.1) into (2.2)–(2.11) and neglecting nonlinear terms in the perturbations, we obtain the linear homogeneous perturbation problem (appendix B). The dispersion relation $\omega = \omega(k; Re, Kn, n)$ is calculated by means of the Chebyshev collocation method (Peyret 2002). This method transforms the perturbation problem into an algebraic eigenvalue problem consisting of a system of $5N$ linear equations satisfied by the perturbations $\rho^{(1)}$, $u_1^{(1)}$, $u_2^{(1)}$, $T^{(1)}$ and $p^{(1)}$ at N discrete points across the gap. Throughout the domain of parameters corresponding to subsequent results, convergence of the calculation is established for $N \approx 15n$, ensuring that a sufficient number of collocation points are distributed along each wavelength of the external force. Unlike DSMC computations (see § 3), there is no difficulty in obtaining results for arbitrarily small $Kn > 0$.

Figure 2 presents the neutral curve (solid line) separating the (Re, Kn) plane into respective domains of stable (unshaded, $\mathrm{Im}\{\omega\} > 0$) and unstable (shaded, $\mathrm{Im}\{\omega\} < 0$) response for $n = 4$, as obtained from the 'slip flow' stability analysis. The corresponding DSMC results, denoted by circles, crosses and squares, mark parameter combinations where the reference state is found to be stable, unstable and marginally stable, respectively. The triangle depicts the critical Reynolds number $Re_{cr} \approx 2.65$ for

the onset of instability according to incompressible analysis in a bounded domain for $n = 4$ (Fukuta & Murakami 1998), and the cross-hatched line marks the critical value $Re_{cr} = \sqrt{2}$ in the counterpart unbounded set-up (Meshalkin & Sinai 1961).

In the incompressible limit ($Kn, Ma \to 0$), the lower left end of the neutral curve coincides with the incompressible bounded-domain solution. For each Re, there exists a maximal value of Knudsen, Kn_{max}, above which the reference state becomes stable. With increasing Kn_{max} between the incompressible limit and $Kn_{max} \approx 0.003\,11$, Re_{cr} increases monotonically from $Re_{cr} \approx 2.65$ to $Re_{cr} \approx 9.4$, respectively. At larger values of Re_{cr}, the maximal Kn for instability decays slowly, reducing to $Kn_{max} \approx 0.003$ at $Re_{cr} = 83$ and $Kn_{max} \approx 0.002\,95$ at $Re_{cr} = 700$. Most remarkably, the neutral curve exhibits a maximum at $Kn_{max} = Kn^* \approx 0.003\,11$, indicating that no instability occurs at $Kn > Kn^*$ for any Re. At this parameter combination, $(Re^*, Kn^*) \approx (9.4, 0.00311)$, the reference pressure is $p^{(0)} \approx 1.97$ (almost twice the pressure in the incompressible problem) and the maximum reference temperature in the middle of the gap $T^{(0)} \approx 2.5$.

The two above phenomena – namely, the occurrence, at a given Kn, of a maximal Re above which the reference state regains its stability, and the existence of a cutoff combination (Re^*, Kn^*) above which instability does not occur – can both be rationalized in terms of the effect of viscous dissipation. According to the scaled form of energy equation (2.4), the viscous dissipation term is proportional to Ma^2/Re_L. Making use of the von Kármán relation (2.12), this is equivalent to proportionality to $Kn^2 Re_L$. Consequently, at a constant Knudsen number, an increase in Re_L (or in Re; see (2.13)) results in an increase in the magnitude of viscous dissipation: kinetic energy is irreversibly transformed into heat, thus cancelling the non-stabilizing impact of increasing the amplitude of the external force. A similar conclusion is drawn when considering the effect of increasing Kn on the system viscous dissipation at a given Re. Evidently, such a mechanism cannot take place in the incompressible problem, where the thermal and dynamical descriptions of the system are decoupled.

Considering the vastly different methods of calculation (linearized eigenvalue problem as opposed to nonlinear initial value statistical simulation), the close agreement between the 'slip flow' and DSMC results is gratifying. The largest differences between the results appear along the upper right portion of the neutral curve, where approximately 10 % discrepancies are obtained. At these (Re, Kn) combinations, elevated gradients in the reference hydrodynamic fields, particularly in the vicinity of the boundaries, are obtained (cf. figure 1*b*). These gradients result in a significant increase in the local Knudsen number, which violates the continuum-limit assumption on which the 'slip flow' model is based. We therefore find the present agreement between the two solutions satisfactory. In particular, the increase in the value of Re_{cr} along the left branch of the neutral curve and the occurrence of a 'cutoff' value for $Kn = Kn^*$ above which the Kolmogorov flow is always stable are confirmed. It is worthwhile to note that the comparison with DSMC calculations is limited to $Kn \gtrsim 0.002$, since numerical simulations become prohibitively time-consuming at lower Kn. Our solution for $Kn < 0.002$ is supported by its convergence to the incompressible limit.

The description of the neutral surface is complemented in figure 3, presenting the variation of the critical wavenumber k_{cr} (normalized by π) with Re_{cr}. The triangle depicts the value of k_{cr} in the incompressible limit (Fukuta & Murakami 1998) and the dashed lines mark two of the wavenumbers ($k/\pi = 4, 5$) included in the discrete spectrum of DSMC calculation (see § 3). Again we note that our solution coincides with the incompressible solution for $Kn \to 0$. For $Kn > 0$, the critical wavenumber varies non-monotonically, first increasing between $k_{cr}/\pi \approx 4.08$

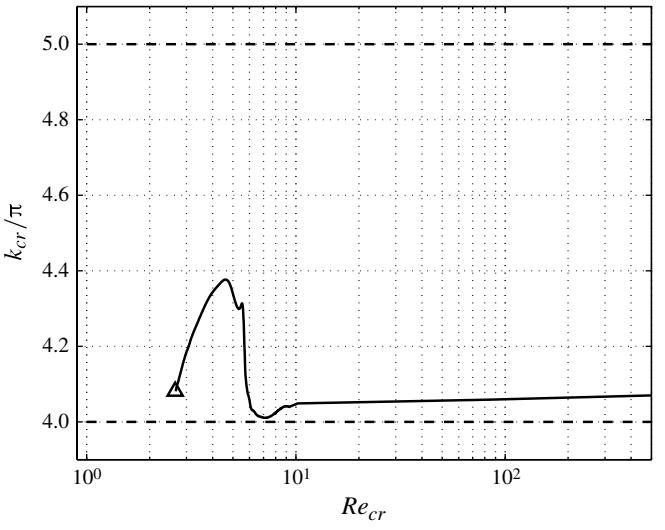

FIGURE 3. Projection of the neutral surface on the $(Re, k/\pi)$ plane for $n = 4$. The solid line depicts the variation with Re_{cr} of the scaled critical wavenumber k_{cr}/π, calculated using 'slip flow' theory. The dashed lines mark two of the wavenumbers ($k/\pi = 4,\ 5$) that are included in the discrete spectrum of DSMC calculation ($k/\pi = 1, 2, \ldots$). The triangle marks the critical value $k_{cr}/\pi \approx 4.08$ in the incompressible problem (Fukuta & Murakami 1998).

and $k_{cr}/\pi \approx 4.37$ for $2.65 \lesssim Re_{cr} \lesssim 4.8$ (corresponding to $0 < Kn_{max} \lesssim 0.0021$), and then decreasing to $k_{cr}/\pi \approx 4.04$ at $Kn = 0.0031$. An abrupt change in k_{cr} is observed near $Re_{cr} \approx 5.65$, accompanied by a 'bump-like' variation in the neutral curve of figure 2 near $Kn_{max} \approx 0.002\,15$. Note that the entire variation of k_{cr} remains close to $k/\pi = 4$ for all Re_{cr}, and we therefore predict the onset of instability in DSMC calculations to be dominated by a wavenumber $k = 4\pi$. This prediction will be confirmed in § 6. (In addition, we have verified that the small deviations of the actual k_{cr} from $k = 4\pi$ have only a minor effect on the calculated neutral curve of figure 2, by calculating the critical curve, according to 'slip flow' analysis, in response to a single perturbation with wavenumber $k = 4\pi$. The differences between the curve obtained and the critical curve in figure 2 were almost indiscernible.)

To further examine the sharp changes in k_{cr} and Kn_{max} near $Re_{cr} \approx 5.65$, figure 4 shows the variation of $\mathrm{Re}\{\omega_{cr}\}$, the frequency of critical perturbations, along the neutral curve. For $Re_{cr} \lesssim 5.65$, our calculations invariably yield imaginary-valued ω. Accordingly, the onset of instability takes place via 'exchange of stabilities' (Chandrasekhar 1961) and is characterized by the appearance of stationary waves. However, at $Re_{cr} \approx 5.65$ the onset of instability changes type to 'overstability', signalized by time-periodic oscillations at a critical frequency $\mathrm{Re}\{\omega_{cr}\} \neq 0$. More specifically, the single mode characterizing the onset of instability in the case of 'exchange of stabilities' is interchanged in the 'overstability' regime by *simultaneous* excitation of *two* eigenmodes, having the same critical frequency with opposite signs. For illustration, this interchange of modes is denoted in the figure by the thin dotted lines. The perturbation field in the case of 'overstability' is obtained by composition of the two excited modes, as demonstrated below (see figures 5*g–i* and 6). The absolute value of the critical frequency is slowly increasing with $Re_{cr} \gtrsim 5.65$.

The onset of instability via 'exchange of stabilities' along the lower left portion of the neutral curve is in accordance with the incompressible-limit result (Meshalkin & Sinai 1961). To validate the bifurcation to 'overstability' at $Kn_{max} \gtrsim 0.0021$,

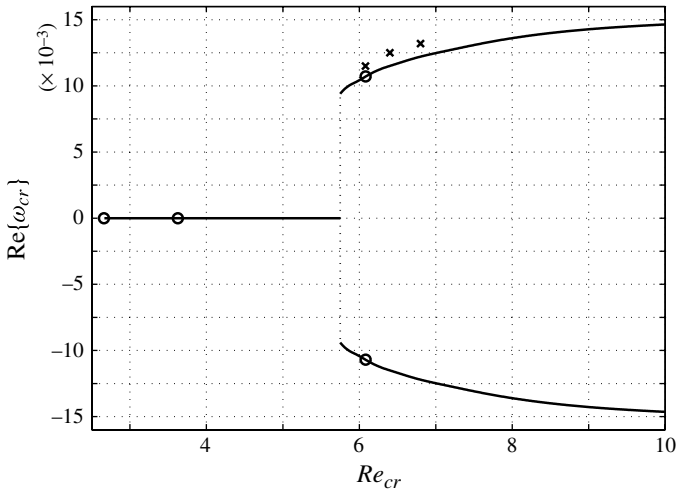

FIGURE 4. Variation of the critical frequency of perturbations $\mathrm{Re}\{\omega_{cr}\}$ at the onset of instability for $n = 4$. At $Re_{cr} \approx 5.65$ (corresponding to $Kn_{max} \approx 0.0021$), the instability changes type from 'exchange of stabilities' (for $Re_{cr} \lesssim 5.65$) to 'overstability' (for $Re_{cr} \gtrsim 5.65$), and the onset of instability is characterized by the excitation of two eigenmodes with opposite-sign eigenfrequencies. The crosses indicate the frequencies of flow field variations observed in DSMC results. The circles denote parameter combinations considered in figure 5. The thin dotted lines mark the interchange between 'exchange of stabilities' ($Re_{cr} \lesssim 5.65$) and 'overstability' ($Re_{cr} \gtrsim 5.65$) modes of instability.

we have examined the time evolution of u_2, the x_2 velocity component, obtained near the onset of instability via DSMC calculations. Indeed, at critical conditions above $Kn_{max} \approx 0.0021$ it was found that u_2 exhibits periodic oscillations. In a quantitative comparison, we examined the flow field at supercritical conditions slightly above the critical conditions $(Re_{cr}, Kn_{max}) \approx (0.0025, 6.08)$, $(0.00265, 6.4)$ and $(0.0028, 6.8)$ found in figure 2. According to DSMC calculations, it was found that $\mathrm{Re}\{\omega_{cr}\} \approx 0.0115$, 0.0125 and 0.0132 (marked by the crosses in figure 4), respectively, which is in good agreement with the results predicted by 'slip flow' theory. In practice, a more detailed comparison with the critical frequencies observed in DSMC computations is hard to obtain, owing to the noisiness of DSMC results near the onset of instability (see § 3). Nevertheless, harmonic time dependence of the solution was observed in all simulations carried out at supercritical conditions with $Kn \gtrsim 0.0021$.

Figure 5 describes the variation of the critical eigenmodes $u_1^{(1)}$, $u_2^{(1)}$ and $T^{(1)}$, as obtained using 'slip flow' theory, along the neutral curve. The figure shows the absolute values of the critical eigenmodes at two parameter combinations where instability sets in via 'exchange of stabilities' (at $Re_{cr} = 2.66$ and 3.63, corresponding to $Kn_{max} = 10^{-5}$ and 0.0017, respectively), and one parameter combination where 'overstability' occurs (at $Re_{cr} = 6.08$, corresponding to $Kn_{max} = 0.0025$). The absolute values of the modes are normalized in each parameter combination by the maximum magnitude of the largest mode.

At the parameter combination closest to the incompressible limit ($(Re_{cr}, Kn_{max}) = (2.66, 10^{-5})$, figure 5*a–c*), the perturbation field is dominated by the velocity perturbations and the temperature fluctuation is vanishingly small. This is in accordance with the decoupling between the momentum and energy equations in this limit, also reflected by the uniformity of the reference temperature and density (see (4.5)). With increasing compressibility effects along the neutral curve, the dynamic and

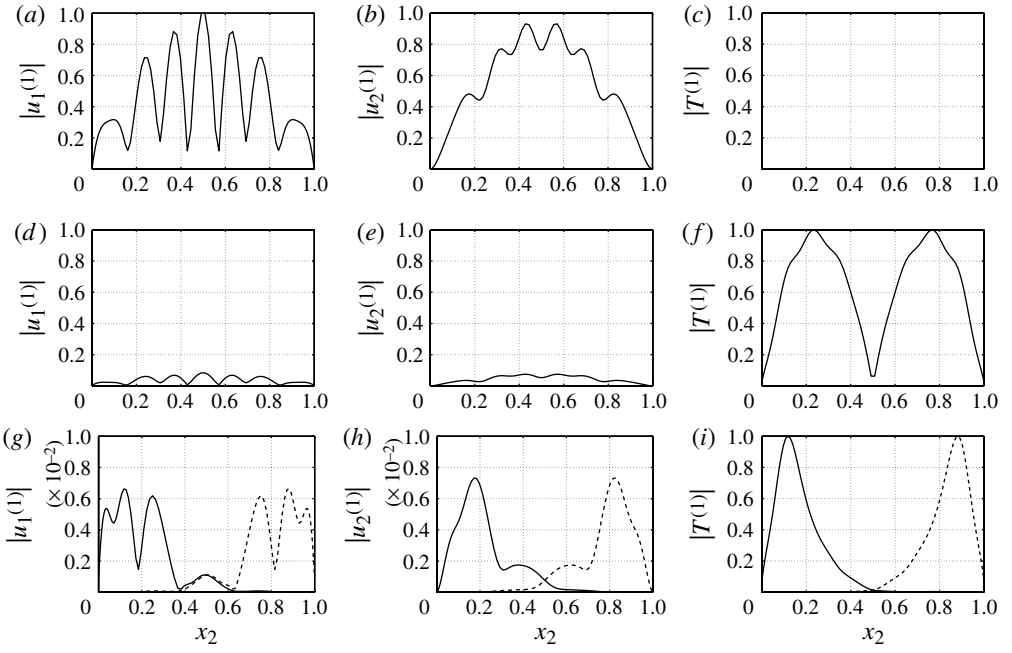

FIGURE 5. Absolute values of the critical eigenmodes $u_1^{(1)}$, $u_2^{(1)}$ and $T^{(1)}$ for $n = 4$ along the neutral curve at (*a–c*) $Re_{cr} = 2.66$, (*d–f*) $Re_{cr} = 3.63$ and (*g–i*) $Re_{cr} = 6.08$. The eigenmodes in each parameter combination are normalized by the maximum value of the largest perturbation.

thermodynamic descriptions of the system become coupled and significant temperature non-uniformities appear in the reference state (see figure 1*b*). As a result, the temperature perturbation at the onset of instability becomes larger, while velocity perturbations decay, as can be seen in figure 5(*d–f*). Once compressibility effects are sufficiently strong, the bifurcation from 'exchange of stabilities' to 'overstability' discussed in figure 4 takes place and instability sets in, in the form of time-harmonic waves. Typical absolute values of the critical eigenfunctions at this stage are shown in figure 5(*g–i*). As described in figure 4, the onset of instability in the 'overstability' regime is characterized by the excitation of two eigenmodes, which are denoted by the solid and dashed lines in figure 5(*g–i*). The absolute values of the two modes are symmetric about $x_2 = 0.5$ and the consequent perturbation field is obtained by their composition. Note that, for clarity of presentation, the scale of velocity perturbations in figure 5(*g*,*h*) has been reduced. In comparison with the temperature perturbation, the magnitude of flow field perturbations keeps decreasing with increasing Re_{cr}. At larger values of Re_{cr}, as well as at supercritical conditions (see § 6), the ratio between temperature and velocity perturbations grows larger, causing the instability to be governed mainly by thermodynamic perturbations. This is in marked contrast with the incompressible limit, where instability is characterized solely by the emergence of convective patterns, which, at large supercritical Reynolds numbers, evolve into two-dimensional turbulence (Green 1974).

6. The instability domain

We now turn to discuss the pattern of instability at supercritical conditions, marked by the shaded zone in figure 2. To analyse the fluctuating part of the hydrodynamic

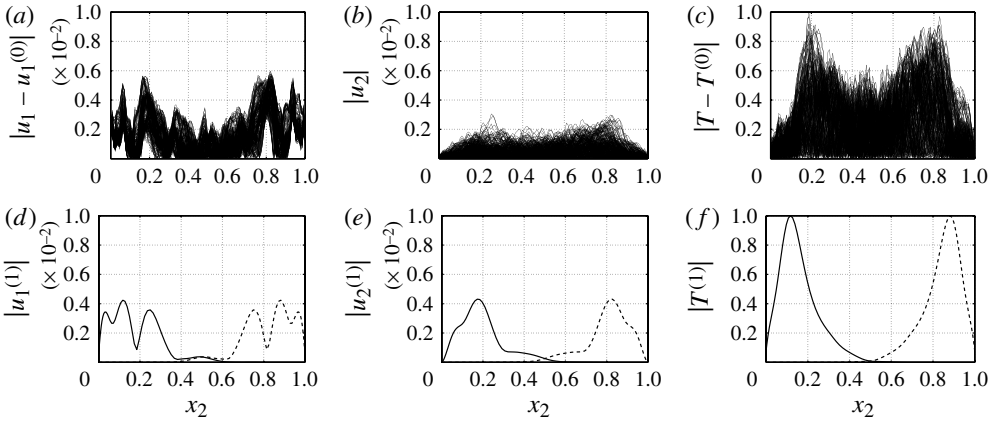

FIGURE 6. Comparison between (*a–c*) the absolute values of the deviations of the velocity and temperature fields from their reference state according to DSMC calculations, and (*d–f*) the absolute values of unstable eigenmodes corresponding to a wavenumber $k = 4\pi$, for $n = 4$ and $(Re, Kn) = (8.37, 0.0025)$.

fields, we subtract the mean fields from the simulation results at each time step of the computation. This can be done either by subtracting the reference fields calculated via the 'slip flow' model, or by deducting the time and space averages of the hydrodynamic fields as calculated from the simulation. In practice, the two procedures give nearly identical results, reconfirming that our continuum-limit model describes well the reference state at the chosen range of parameters.

Figure 6 compares the excess of DSMC solution over the reference state, calculated as described above (figure 6*a–c*), and the eigenmodes excited in response to a perturbation of $k = 4\pi$ (figure 6*d–f*) according to the 'slip flow' theory. The comparison is made at the supercritical conditions $n = 4$ and $(Re, Kn) = (8.37, 0.0025)$ (see figure 2). Each curve in figure 6(*a–c*) denotes an x_2 distribution of the respective perturbation according to DSMC solution, at a specific value of $0 \leqslant x_1 \leqslant 2$ along the computation domain. The results are scaled as in figure 5, by dividing all the fields by the respective maximum magnitude of the largest perturbation.

The combination of parameters considered in figure 6 is only slightly above the critical conditions, to enable a qualitative comparison between the simulated perturbation fields and linear-analysis predictions. Following the description in figure 5(*g–i*) of the 'overstability' mechanism of instability, the calculation based on the 'slip flow' scheme yields two unstable eigenfunctions with equal growth rates ($|\mathrm{Im}\{\omega\}| \approx 7 \times 10^{-4}$) and opposite-sign frequencies ($\mathrm{Re}\{\omega\} \approx \pm 0.0125$). Comparing figure 6(*a–c*) and figure 6(*d–f*), the general forms of eigenmodes and DSMC perturbation fields are very similar, particularly for the temperature. This similarity is satisfactory, recalling that the linear stability analysis is not expected to yield the final form of perturbations (see Introduction). The simulation also confirms that the deviation of the temperature field over its mean value is typically the largest, dominating the velocity-field perturbations, as predicted by figure 5 at the onset of instability.

Figure 7 presents the variation with Re of the perturbation flow field according to DSMC results, for $n = 4$ and $Kn = 0.0025$. Figure 7(*a–c*) shows time snapshots of the time-periodic perturbation flow field. To quantify the relative strength of velocity

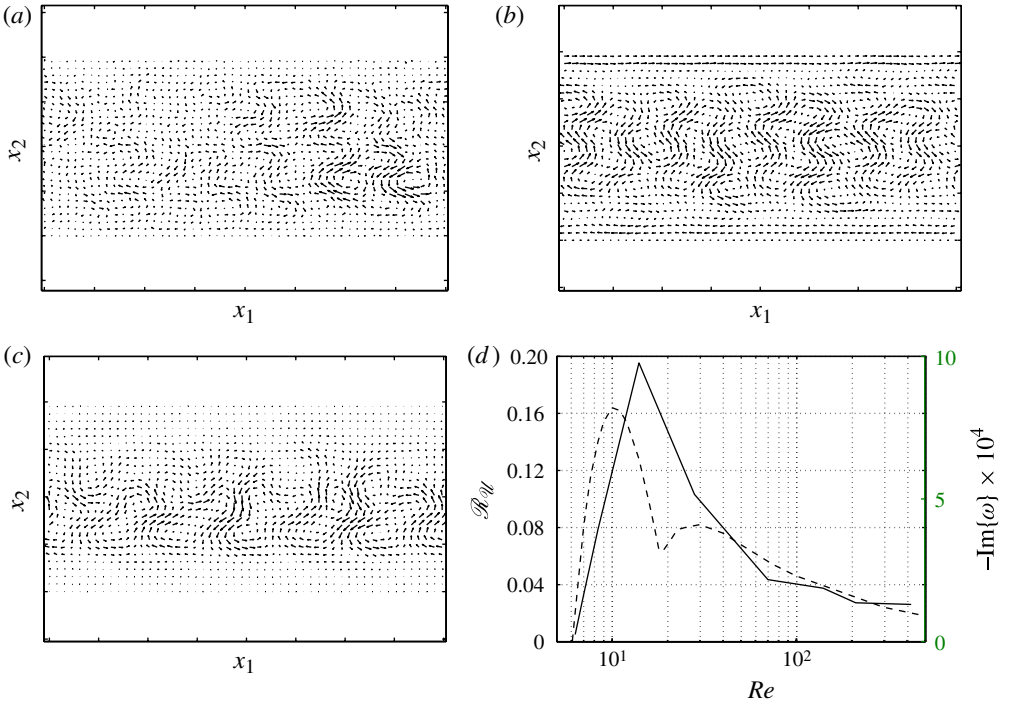

FIGURE 7. Time snapshots of the velocity perturbation vector fields, calculated using the DSMC method, for $n = 4$, $Kn = 0.0025$ and (*a*) $Re = 7$, (*b*) $Re = 13.9$ and (*c*) $Re = 139$. (*d*) Variation with Re of the velocity ratio $\mathscr{R}_{\mathscr{U}}$ (see (6.1)) calculated using the DSMC method (solid line), and the growth rate of perturbations at a wavenumber $k = 4\pi$ (dashed line), for $n = 4$ and $Kn = 0.0025$.

perturbations, we introduce

$$\mathscr{R}_{\mathscr{U}} \equiv \frac{\max\{|u_2|\}}{\max\{|u_1|\}}, \tag{6.1}$$

describing the ratio between the maximum velocity in the x_2 direction (which is non-zero only when the reference state is unstable) and the maximum velocity in the x_1 direction. The solid line in figure 7(*d*) shows the variation with Re of $\mathscr{R}_{\mathscr{U}}$ at $n = 4$ and $Kn = 0.0025$, and the dashed line presents the respective growth rate (in negative sign) of perturbations corresponding to a wavenumber $k = 4\pi$, as calculated by the 'slip flow' scheme.

Starting with figure 7(*a*), we observe that, slightly above the instability threshold ($Re = 7 > Re_{cr} \approx 6.08$), the perturbation flow field contains weak vortical patterns occupying most of the gas layer. The respective values of $\mathscr{R}_{\mathscr{U}}$ and perturbation growth rate are small. With increasing $6.08 \lesssim Re \lesssim 10$, coherent convective rolls are formed and their relative strength grows, reaching a maximum at $Re \approx 10$ according to both DSMC and linear-theory results (cf. the solid and dashed lines in figure 7*d*). A typical picture of the flow field at this stage is shown in figure 7(*c*). With Re increasing further, the relative strength of convective rolls decays, and the vortices become somewhat confined to a narrower layer in the middle of the gap.

According to figure 7(*a–c*), and throughout the range of parameters simulated, it was found that instability is always characterized by a wavenumber of $k = 4\pi$.

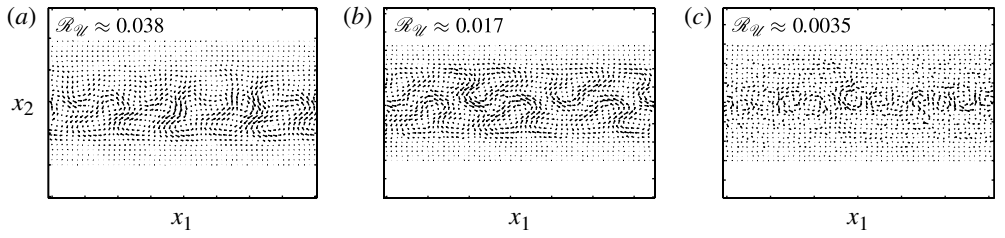

FIGURE 8. Time snapshots of the velocity perturbation vector fields, calculated using the DSMC method, for $n = 4$, $Re = 139$ and (a) $Kn = 0.0025$, (b) $Kn = 0.003125$ and (c) $Kn = 0.0033$. The respective values of $\mathscr{R}_{\mathscr{U}}$ are indicated at the top of each panel.

This is supported by the linear analysis results (see figure 3), showing that all other wavenumbers included in the discrete DSMC spectrum ($k = \pi n$, $n = 1, 2, \ldots$) correspond to either decaying (stable) modes or modes with lower growth rates. In general, we also note that the decrease in perturbation growth rate at large Re (e.g. at $Re \gtrsim 10$ for the case $Kn = 0.0025$ presented in figure 7d) is very slow, resulting in the extension of the instability domain to very large Reynolds numbers (outside the range presented in figure 2 for $Kn = 0.0025$). Typically, however, the vortical motion at large Re becomes nearly invisible and confined to the middle of the gap, while most of the gas domain remains 'dynamically stable'.

Figure 8 describes the variation with Kn of the perturbation flow field, calculated using the DSMC method, for $n = 4$ and $Re = 139$. As in figure 7, the figure shows time snapshots of the time-periodic perturbation flow fields. The respective values of $\mathscr{R}_{\mathscr{U}}$ are indicated at the top of each figure. Figure 8(a) (for $Kn = 0.0025$) is identical to figure 7(c) for easy reference. With increasing Kn at constant Re, compressibility effects become stronger (see (2.12)). Consequently, the system is stabilized and the value of $\mathscr{R}_{\mathscr{U}}$ diminishes. At $Kn > Kn_{max}$, the reference state recovers its stability. According to 'slip flow' theory, $Kn_{max} \approx 0.003$ for the present $Re = 139$, while DSMC calculations predict $Kn_{max} \approx 0.0033$. The DSMC perturbation flow field in the latter case is presented in figure 8(c). For this parameter combination, denoted by a square in figure 2, the system exhibits 'marginal stability' behaviour, characterized by irregular velocity perturbations. These perturbations are an order of magnitude lower than the coherent patterns observed in figure 8(a). At $Kn > Kn_{max}$, these perturbations vanish and the reference state is stable.

7. The case $n \gg 1$

In the incompressible analysis of Meshalkin & Sinai (1961), it was shown that the critical Reynolds number for instability in an unbounded domain is $Re_{cr} = \sqrt{2}$, regardless of the forcing signal wavenumber. Later on, Fukuta & Murakami (1998) found that the effect of bounding surfaces at finite n is to stabilize the system by increasing the value of Re_{cr}. However, in the limit $n \to \infty$ it was shown that the impact of the walls vanishes and the critical Reynolds number obtains its unbounded limit. In this section we examine the effect of fluid compressibility on this result.

Figure 9 presents a comparison between the neutral curves in the (Re, Kn) domain, obtained using 'slip flow' theory, for $n = 4$ (dashed line, identical to the solid line in figure 2) and $n = 10$ (solid line). As in figure 2, the triangles and cross-hatched line mark the critical Reynolds numbers in the bounded and unbounded incompressible problems, respectively.

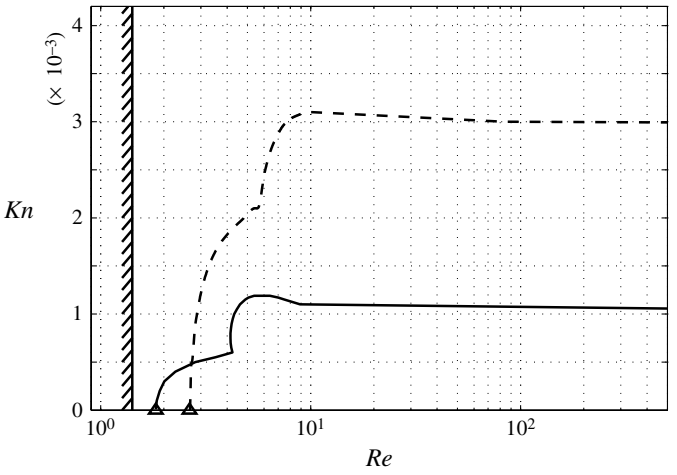

FIGURE 9. Comparison between the neutral curve in the (Re, Kn) plane for $n = 4$ (dashed line) and $n = 10$ (solid line) obtained using 'slip flow' theory. The triangles and cross-hatched line mark the critical Reynolds numbers calculated in the incompressible bounded (Fukuta & Murakami 1998) and unbounded (Meshalkin & Sinai 1961) problems, respectively.

At first we observe that the lower left part of the neutral curve approaches the incompressible limit in an unbounded domain with increasing n, in accordance with the result of Fukuta & Murakami (1998). This is accompanied by a decrease in the critical wavenumber (not presented here), which, in the unbounded problem, obtains the limit $k_{cr} = 0$ (infinitely long waves). The general form of the neutral curve for both n is similar, with Kn_{max} increasing with Re_{cr} along the left branch, and then decaying slowly. Both curves exhibit a maximum at some $Kn = Kn^*$ above which the reference state is stable for all Re. A 'bifurcation point' at the 'bump' of the left branch, where the onset of instability changes type from 'exchange of stabilities' to 'overstability' (see § 5), is found in both cases.

The most significant difference between the two curves is the confinement of instability domain to lower Kn at larger n. This suggests that, unlike in the incompressible bounded problem, the effect of isothermal boundaries at $n \to \infty$ remains *finite*, and the neutral curve does not converge to the unbounded-limit criterion of Meshalkin & Sinai (1961) for $Kn > 0$. Interestingly, when rescaling the Knudsen number by n (which is equivalent to basing Kn on the external force wavelength instead of the layer width L), the two curves possess a maximum at a similar value of $n\,Kn^*$. The respective value of Re^*, though, still shifts at larger n to lower Re (closer to $Re_{cr} = \sqrt{2}$), owing to the vanishing effect of the boundaries in the incompressible limit.

In practice, even the 'slip flow' scheme (and, by far, the DSMC calculation at the extremely low Knudsen numbers considered) becomes numerically expensive at large n, owing to the large number of collocation points required along each of the $n \gg 1$ wavelengths of the periodic force (see § 5). To overcome this difficulty and gain further insight into the limit $n \to \infty$, the above-mentioned 'rescaling' mechanism of replacing Kn with $n\,Kn^*$ may empower application of the method of asymptotic homogenization, where the various fields are expanded in a long scale (the layer width L; see e.g. the reference temperature in figure 1*b*) and a short scale (L/n; e.g. the reference velocity in figure 1*a*). As n increases, the forcing wavelength L/n

decreases, causing the Knudsen number $n\,Kn$ based on this length scale (at a fixed L) to become larger. While this may invalidate the application of the slip flow scheme at $n \gg 1$, we note again that, according to figure 9, increasing n results in confinement of the neutral curve to lower Kn^*; consequently, the respective wavelength-based Knudsen number $n\,Kn^*$ remains similar to its value at lower n. The continuum-limit assumption is therefore not violated, and the proposed analysis may be carried out to shed light on the differences between the incompressible and compressible problems at large forcing wavenumbers. This is a topic of a work in progress.

8. Concluding comments

We studied the effect of flow compressibility on the two-dimensional temporal stability of a layer of hard-sphere gas confined between two isothermal walls and subject to a spatially periodic external force. Compressibility was found to affect the flow pattern mainly through the irreversible transfer of gas kinetic energy into heat, leading to elevated temperature levels in the bulk of the gas. This, in turn, has a significant stabilizing impact on the system, resulting in an increase in the critical Reynolds number for instability, and a change in the type of instability observed, from 'exchange of stabilities' (close to the incompressible limit) to 'overstability' (when compressibility is strong enough). Most remarkably, gas compressibility, combined with the viscous (incompressible) mechanism for instability, confines the instability domain to small ($O(10^{-3})$) Knudsen numbers.

It is commonly accepted that flows at $Kn \lesssim O(10^{-3})$ are well described by means of the continuum description. It could therefore be speculated that the stability problem studied here may be analysed by means of continuum Navier–Stokes equations with no-slip conditions. However, as observed in figures 1, 5 and 6, while the *global* Knudsen numbers considered are indeed small, significant temperature jump and velocity slip amplitudes are found at the boundaries. This is due to the large local gradients obtained in the vicinity of the walls, which result in decrease in the local length scale and increase in the *local* Knudsen number. Consistent modelling of the compressible flow problem must therefore take into account the effect of gas rarefaction.

The present work presents a two-dimensional analysis of the compressible Kolmogorov flow, and is based on a comparison between linear 'slip flow' theory and DSMC computations. In a three-dimensional set-up, both slip flow scheme and particularly DSMC calculations become considerably more involved. According to Squire's theorem (Squire 1933), the critical conditions for the onset of instability in incompressible parallel flows are governed by two-dimensional disturbances. However, this result has not been extended to consider compressible flows. It is therefore possible that the onset of instability in the compressible Kolmogorov problem is governed, at some point, by three-dimensional disturbances. In accordance with Squire's theorem, the critical conditions in the incompressible limit (i.e. close to the lower left part of the neutral curve of figure 2) are determined by two-dimensional analysis, and it therefore seems likely that two-dimensional disturbances should also govern the critical behaviour at weakly compressible conditions. Yet, this statement requires further investigation. Since three-dimensional DSMC calculations are beyond the current computational ability of our system, a study of the full three-dimensional compressible problem is deferred to a later contribution, where a comparison between the two methods of solution would be feasible.

The main contribution of the present work is in analysing the stabilizing effect of gas compressibility on bounded Kolmogorov flow. A similar effect was found in other analyses of rarefied gas flows, including the Rayleigh–Bénard (Stefanov *et al.* 2002; Manela & Frankel 2005) and Taylor–Couette (Yoshida & Aoki 2006; Manela & Frankel 2007) problems. Interestingly, it was shown that suppression of instability in the Taylor–Couette problem is brought about by increased rates of dissipation associated with aerodynamic heating of the fluid, similarly to what has been observed in the present study. The common conclusion of these works may therefore be that non-zero gas rarefaction rates (which combine gas viscosity and compressibility, in accordance with the von Kármán relation (2.12)) result in stabilization of gas flow systems, and confine hydrodynamic instability phenomena to the continuum limit of small Knudsen numbers.

Acknowledgements

Part of this work was supported by the National Natural Science Foundation of China (Grant Nos. 10921062 and 11002147). We thank Professor J. Fan for his support and helpful comments during this work.

Appendix A. Solutions for $u_{1_\varepsilon}^{(0)}$ and $u_{1_{Kn}}^{(0)}$ in (4.8)

The solutions for $u_{1_\varepsilon}^{(0)}$ and $u_{1_{Kn}}^{(0)}$ are obtained from a double x_2 integration of the $O(\varepsilon)$ and $O(Kn)$ momentum equation (4.1), respectively, and satisfaction of the respective orders of slip boundary condition (4.4). This procedure yields (4.8), where

$$a_1 = -f(1), \quad b_0 = \frac{1.1466}{2\pi n}, \quad b_1 = -\frac{1.1466}{\pi n} \tag{A 1}$$

and

$$f(x_2) = \int_0^{x_2}\int_0^{s}\left[\frac{2\pi^2 n^2}{9}\sin(2\pi np)\left(-3p^2+3p-\frac{1}{3}-\frac{1-3\cos(4\pi np)}{8\pi^2 n^2}\right)\right.$$
$$\left. + \frac{\pi n}{9}\cos(2\pi np)\left(2p-1+\frac{\sin(4\pi np)}{2\pi n}\right)\right]\mathrm{d}p\,\mathrm{d}s. \tag{A 2}$$

A closed-form expression for the double integral (A 2) can be easily calculated, but is skipped here for brevity.

Appendix B. The linearized perturbation problem

To simplify notation we omit in the following the superscripts (1) in the expressions of the perturbations. The resulting perturbation problem, in terms of the parameters Re_L, Ma and Kn, consists of the continuity,

$$\mathrm{i}\omega\rho + \rho^{(0)}\left(\mathrm{i}ku_1 + \frac{\mathrm{d}u_2}{\mathrm{d}x_2}\right) + \mathrm{i}ku_1^{(0)}\rho + \frac{\mathrm{d}\rho^{(0)}}{\mathrm{d}x_2}u_2 = 0, \tag{B 1}$$

x_1 momentum,

$$\rho^{(0)}\left(\mathrm{i}\omega u_1 + \mathrm{i}ku_1^{(0)}u_1 + \frac{\mathrm{d}u_1^{(0)}}{\mathrm{d}x_2}u_2\right) = -\frac{3\mathrm{i}k}{5Ma^2}p + \frac{1}{Re_L}\sigma_{x_1} + \frac{\sin(2\pi nx_2)}{Re_L}\rho, \tag{B 2}$$

x_2 momentum,

$$\rho^{(0)}\left(\mathrm{i}\omega u_2+\mathrm{i}ku_1^{(0)}u_2\right)=-\frac{3}{5Ma^2}\frac{\mathrm{d}p}{\mathrm{d}x_2}+\frac{1}{Re_L}\sigma_{x_2} \tag{B 3}$$

and energy

$$\rho^{(0)}\left(\mathrm{i}\omega T+\mathrm{i}ku_1^{(0)}T+\frac{\mathrm{d}T^{(0)}}{\mathrm{d}x_2}u_2\right)=-\frac{5}{2Re_L}h-\frac{2C}{3}\left(\mathrm{i}ku_1+\frac{\mathrm{d}u_2}{\mathrm{d}x_2}\right)+\frac{10Ma^2}{9Re_L}D, \tag{B 4}$$

equations, together with the equation of state

$$p=\rho^{(0)}T+T^{(0)}\rho. \tag{B 5}$$

The perturbation problem is supplemented by the boundary conditions (see (2.11))

$$u_2=0,\quad u_1=\pm\zeta\frac{\partial u_1}{\partial x_2},\quad T=\pm\tau\frac{\partial T}{\partial x_2}\quad \text{at } x_2=\begin{bmatrix}0\\1\end{bmatrix}. \tag{B 6}$$

Here, the normalization condition (the homogeneous counterpart of (2.10)) is trivially satisfied by the periodic x_1 dependence of the density perturbation. In the viscous-stress terms of (B 2) and (B 3),

$$\begin{aligned}\sigma_{x_1}=&\frac{\mathrm{d}}{\mathrm{d}x_2}\left(\frac{\mathrm{d}u_1^{(0)}}{\mathrm{d}x_2}\frac{T}{2\sqrt{T^{(0)}}}\right)-\frac{2\sqrt{T^{(0)}}}{3}\left(2k^2u_1+\mathrm{i}k\frac{\mathrm{d}u_2}{\mathrm{d}x_2}\right)\\&+\frac{\mathrm{d}}{\mathrm{d}x_2}\left[\sqrt{T^{(0)}}\left(\frac{\mathrm{d}u_1}{\mathrm{d}x_2}+\mathrm{i}ku_2\right)\right]\end{aligned} \tag{B 7}$$

and

$$\begin{aligned}\sigma_{x_2}=&\frac{\mathrm{i}k}{2\sqrt{T^{(0)}}}\frac{\mathrm{d}u_1^{(0)}}{\mathrm{d}x_2}T+\sqrt{T^{(0)}}\left(\mathrm{i}k\frac{\mathrm{d}u_1}{\mathrm{d}x_2}-k^2u_2\right)\\&+\frac{2}{3}\frac{\mathrm{d}}{\mathrm{d}x_2}\left[\sqrt{T^{(0)}}\left(-\mathrm{i}ku_1+2\frac{\mathrm{d}u_2}{\mathrm{d}x_2}\right)\right].\end{aligned} \tag{B 8}$$

In the heat flux and dissipation terms in (B 4),

$$h=k^2\sqrt{T^{(0)}}T-\frac{\mathrm{d}}{\mathrm{d}x_2}\left(\sqrt{T^{(0)}}\frac{\mathrm{d}T}{\mathrm{d}x_2}+\frac{1}{2\sqrt{T^{(0)}}}\frac{\mathrm{d}T^{(0)}}{\mathrm{d}x_2}T\right) \tag{B 9}$$

and

$$D=2\sqrt{T^{(0)}}\frac{\mathrm{d}u_1^{(0)}}{\mathrm{d}x_2}\left(\frac{\mathrm{d}u_1}{\mathrm{d}x_2}+\mathrm{i}ku_2\right)+\frac{1}{2\sqrt{T^{(0)}}}\left(\frac{\mathrm{d}u_1^{(0)}}{\mathrm{d}x_2}\right)^2T, \tag{B 10}$$

respectively.

REFERENCES

ARNOL'D, V. I. & MESHALKIN, L. D. 1960 A. N. Kolmogorov's seminar on selected problems of analysis (1958/1959). *Usp. Mat. Nauk* **15**, 247–250 (in Russian).

BENA, I., MALEK MANSOUR, M. & BARAS, F. 1999 Hydrodynamic fluctuations in the Kolmogorov flow: linear regime. *Phys. Rev.* E **59**, 5503–5510.

BIRD, G. 1994 *Molecular Gas Dynamics and the Direct Simulations of Gas Flows*. Clarendon Press.

BURGESS, J. M., BIZON, C., MCCORMICK, W. D., SWIFT, J. B. & SWINNEY, H. L. 1999 Instability of the Kolmogorov flow in a soap film. *Phys. Rev.* E **60**, 715–721.

CHANDRASEKHAR, S. 1961 *Hydrodynamic and Hydromagnetic Stability*. Clarendon Press.

FUKUTA, H. & MURAKAMI, Y. 1998 Side-wall effect on the long-wave instability in Kolmogorov flow. *J. Phys. Soc. Japan* **67**, 1597–1602.

GOLSHTEIN, E. & ELPERIN, T. 1996 Convective instabilities in rarefied gases by direct simulation Monte Carlo method. *J. Thermophys. Heat Transfer* **10**, 250–256.

GREEN, J. S. A. 1974 Two-dimensional turbulence near the viscous limit. *J. Fluid Mech.* **62**, 273–287.

VON KÁRMÁN, T. 1963 *From Low-Speed Aerodynamics to Astronautics*. Pergamon Press.

MANELA, A. & FRANKEL, I. 2005 On the Rayleigh–Bénard problem in the continuum limit. *Phys. Fluids* **17**, 036101.

MANELA, A. & FRANKEL, I. 2007 On the compressible Taylor–Couette problem. *J. Fluid Mech.* **588**, 59–74.

MESHALKIN, L. D. & SINAI, IA. G. 1961 Investigation of the stability of a stationary solution of a system of equations for the plane movement of an incompressible viscous fluid. *Prikl. Mat. Mekh.* **25**, 1140–1143.

PEYRET, R. 2002 *Spectral Methods for Incompressible Viscous Flow*. Springer.

PLATT, N., SIROVICH, L. & FITZMAURICE, N. 1991 An investigation of chaotic Kolmogorov flows. *Phys. Fluids* A **3**, 681–696.

SHE, Z. S. 1987 Metastability and vortex pairing in the Kolmogorov flow. *Phys. Lett.* A **124**, 161–164.

SIVASHINSKY, A. 1985 Weak turbulence in periodic flows. *Physica* D **17**, 243–255.

SOMMERIA, J. 1986 Experimental study of the two-dimensional inverse energy cascade in a square box. *J. Fluid Mech.* **170**, 139.

SONE, Y. 2002 *Kinetic Theory and Fluid Dynamics*. Birkhauser.

SQUIRE, H. B. 1933 On the stability for three-dimensional disturbances of viscous fluid flow between parallel walls. *Proc. R. Soc.* **A142**, 621–628.

STEFANOV, S. & CERCIGNANI, C. 1993 Monte Carlo simulation of the Taylor–Couette flow of a rarefied gas. *J. Fluid Mech.* **256**, 199–213.

STEFANOV, S., ROUSSINOV, V. & CERCIGNANI, C. 2002 Rayleigh–Bénard flow of a rarefied gas and its attractors. I. Convection regime. *Phys. Fluids* **14**, 2255–2269.

STEFANOV, S., ROUSSINOV, V. & CERCIGNANI, C. 2007 Rayleigh–Bénard flow of a rarefied gas and its attractors. III. Three-dimensional computer simulations. *Phys. Fluids* **19**, 124101.

TABELING, P., PERRIN, B. & FAUVE, S. 1987 Instability of a linear array of forced vortices. *Europhys. Lett.* **3**, 459–465.

THESS, A. 1992 Instabilities in two-dimensional spatially periodic flows. Part I. Kolmogorov flow. *Phys. Fluids* A **4**, 1385–1395.

TSIEN, H. S. 1946 Similarity laws of hypersonic flows. *J. Math Phys.* **25**, 247–252.

YOSHIDA, H. & AOKI, K. 2006 Linear stability of the cylindrical Couette flow of a rarefied gas. *Phys. Rev.* E **73**, 021201.

ZHANG, J. & FAN, J. 2009 Monte Carlo simulation of thermal fluctuations below the onset of Rayleigh–Bénard convection. *Phys. Rev.* E **79**, 056302.

ZHANG, J. & FAN, J. 2011 Monte Carlo Simulation of two-dimensional Kolmogorov flow. In *Rarefied Gas Dynamics* (ed. D. A. Levin, I. J. Wysong & A. L. Garcia), pp. 378–383. American Institute of Physics.